Generated using the official AMS LATEX template v6.1



# **Energetics and Transfer of Submesoscale Brine Driven Eddies at a Sea Ice**

## Edge

Anna Lo Piccolo,<sup>a</sup> Christopher Horvat,<sup>a,b</sup> and Baylor Fox-Kemper<sup>a</sup>

<sup>a</sup> Department of Earth, Environmental, and Planetary Sciences, Brown University, Providence, RI, USA

<sup>b</sup> Department of Physics, University of Auckland, Auckland, NZ

Corresponding author: Anna Lo Piccolo, anna\_lo\_piccolo@brown.edu

1

**Early Online Release:** This preliminary version has been accepted for publication in *Journal of Physical Oceanography*, may be fully cited, and has been assigned DOI 10.1175/JPO-D-23-0147.1. The final typeset copyedited article will replace the EOR at the above DOI when it is published.

© 2024 American Meteorological Society. This is an Author Accepted Manuscript distributed under the terms of the default AMS reuse license. For information regarding reuse and general copyright information, consult the AMS Copyright Policy (www.ametsoc.org/PUBSReuseLicenses).

ABSTRACT: During polar winter, refreezing of exposed ocean areas results in the rejection of brine, i.e., salt-enriched plumes of water, a source of available potential energy that can drive ocean instabilities. As this process is highly localized, and driven by sea ice physics, not gradients in oceanic or atmospheric buoyancy, it is not currently captured in modern climate models. This study aims to understand the energetics and lateral transfer of density at a semi-infinite, instantaneously-opened and continuously re-freezing sea ice edge through a series of high resolution model experiments. We show that kilometer-scale submesoscale eddies grow from baroclinic instabilities via an inverse energy cascade. These eddies meander along the ice edge and propagate laterally. The lateral transfer of buoyancy by eddies is not explained by existing theories. We isolate the fundamental forcing-independent quantities driving lateral mixing, and discuss the implications for the overall strength of submesoscale activity in the Arctic Ocean.

#### 1. Introduction

The mixing and subsequent evolution of the upper polar oceans is a critical component of the polar Earth system and its coupling to lower latitudes. The polar oceans are distinct due to their seasonally periodic sea ice cover, which controls the exchange of momentum, water, and heat with the atmosphere compared to open water. The sea ice cover itself is a mosaic of many individual pieces, known as floes. Large consolidated regions of sea ice floes (or floe agglomerations) crack under mechanical stresses, creating leads, long, narrow, near-linear areas of open water, up to hundreds of kilometers long and up to tens of kilometers wide. These leads emerge dynamically and episodically and are key features of the large-scale sea ice cover (Fily and Rothrock 1990; Lindsay and Rothrock 1995; Schulson 2004; Hutter et al. 2019). At synoptic scales, over many leads and floe configurations, sea ice provides an intermittent forcing partly related to sea ice thermodynamics and partly related to sea ice mechanics. The combination of these processes is challenging to reproduce in global climate models, which are not able to represent temperature and salinity profiles in the Arctic Ocean (Steiner et al. 2004; Rosenblum et al. 2021). A better understanding of ocean mixing processes under sea ice is necessary to reflect the influence of brittle, fractured sea ice cover on sub-climate-model-grid-scales (Herman 2022; Shrestha and Manucharyan 2022; Horvat 2022).

During winter, when openings form in sea ice, low atmospheric temperatures cause large heat fluxes out of the exposed ocean, so that new sea ice grows rapidly in the opening. As new ice forms, dense, salt-enriched water is rejected from the growing ice lattice. This process, known as brine rejection, plays a critical role in determining the structure and forcing of the Arctic Ocean variability (Wettlaufer et al. 1997; Aagaard and Carmack 1989). Brine rejection triggers vertical convective mixing, leading to a cross-ice-edge gradient in density over the convective layer depth. This is an actively-forced, sub-climate-model-grid-scale process, different from typical mesoscale spindown processes studied in ice free regions (Boccaletti et al. 2007; Fox-Kemper et al. 2008).

A number of previous studies, conducted via laboratory experiments and idealized numerical model simulations, explore the dynamics of the ice-covered oceans at a lead, typically driven

by an imposed flux of salt at the ocean surface. They suggest the formation of eddies along the fronts at the sea ice edges (Bush and Woods 2000; Smith IV et al. 2002; Matsumura and Hasumi 2008; Cohanim et al. 2021). An important focus of these studies is to derive governing relationships between the ocean deformation radius, frontal length scale and eddy size, and their sensitivity to model parameters, such as lead width and the duration of the imposed forcing (Smith IV et al. 2002; Matsumura and Hasumi 2008; Cohanim et al. 2021).

By measuring the spectral slope of horizontal potential density variance in the Arctic Ocean and comparing it with the typical spectra of mid-latitudes, which decays as  $k^{-2}$  (Callies and Ferrari 2013; Fox-Kemper et al. 2011), some observations indicate that upper-ocean variability under sea ice is weaker than in mid-latitudes (Timmermans et al. 2012; Mensa and Timmermans 2017). Others seem to indicate that the energetics of the Arctic Ocean submesoscale is more important than expected (Mensa et al. 2018). Evidence of a vigorous upper-ocean eddy regime has been found in both marginal ice zones and in the ice pack, by drifter measurements in the Beaufort Sea (Timmermans et al. 2012; Mensa and Timmermans 2017; Mensa et al. 2018) and elsewhere under sea ice by other methods (Brenner et al. 2020; Swart et al. 2020; Biddle and Swart 2020; Giddy et al. 2021).

In this work, given the complexity of ice-ocean interactions, we take a step back. Instead of considering a lead, where resulting ocean dynamics emerges due to the coupling of two ice boundaries, we study the sub-mesoscale dynamics that emerges along an idealized single ice edge where brine rejection occurs. In this way, we develop a theoretical framework from which the understanding of the more complex system of two coupled sea-ice edges could be built. The study of the dynamics under a lead is intentionally left for future work. We further neglect the role of sea-ice dynamics, exploring a thermodynamics-only regime in freezing conditions.

The main two goals of this work are to understand: (1) how actively forced, brine-driven submesoscale eddies differ from those generated by frontal spindown in the mid-latitudes, and (2) the key length and time scalings of the front and eddy evolution. By doing so, we hope to begin to address open questions about the scaling and importance of sub-grid eddy variability driven by brine rejection variability across sea ice boundaries. We use hydrostatic general ocean

circulation simulations coupled with an active thermodynamic sea ice model initialized with an idealized ice edge under freezing conditions. Studying their energetics, we show how brine-driven eddies are inherently different from the initial condition frontal adjustment problem valid for mid-latitudes and used to develop the Fox-Kemper et al. (2008) (hereafter FFH) mixed-layer eddy (MLE) parameterization (Fox-Kemper et al. 2011; Bodner et al. 2023). We then address the analysis of length scales in the ice-edge problem with reference to the work of Matsumura and Hasumi (2008) (hereafter MH), showing that the MH scaling underestimates the eddy-driven frontal expansion in a continuously-evolving experiment, and providing new estimates that track the evolving front. By doing so, we interpret and alleviate conflicts among previous assessments of the scaling of brine-driven submesoscale eddies. The study of a single sea ice edge system allows for a comparison with mid-latitude fronts under overturning (see Sec. 5a). Future efforts will extend this work to the study of two neighboring sea ice edges forming a lead (Sec. 6). This work is not an attempt to suggest new parameterizations for under-ice ocean processes, rather an exploration of the ocean dynamics at a sea ice edge, which highlights important complexities that need to be considered when moving to a more realistic sea ice-ocean model.

The paper structure is as follows. Sec. 2 introduces the methods, model description, and experimental design. Sec. 3 presents the theoretical ice-edge framework and the study of the brine-driven eddy energetics. Sec. 4 examines the scaling of the frontal dynamics. Sec. 5 discusses results in the context of the assumptions behind the FFH parameterization for midlatitude submesoscale eddies and then explores the sensitivity to external forcing. The paper is summarized in Sec. 6.

#### 2. Methods

For this study we use the MIT general circulation ocean model (MITgcm: Marshall et al. 1997) in a hydrostatic, Boussinesq approximation, since the Arctic Ocean dynamics on the scale of 100s of meters under brine rejection is mainly hydrostatic (Smith IV and Morison 1998). Atmospheric turbulent fluxes are computed using a version of the CheapAML (Deremble et al. 2013) atmospheric mixed-layer model over sea ice (Horvat et al. 2016) using a specified climatolgical temperature field. Sea ice is modeled using the thermodynamic sea ice package of

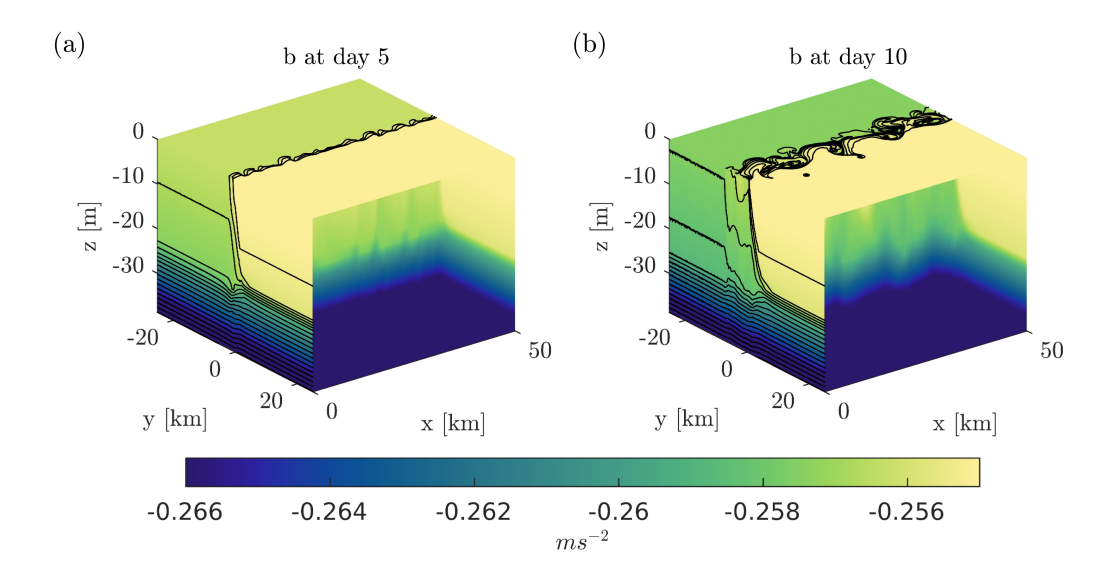


Fig. 1. Three-dimensional visualization of the buoyancy field in the REF experiment at days 5 (a) and 10 (b). Only the first 38 meters depth of the ocean domain are shown. Contour lines of buoyancy are shown only on the yz and top xy slices. Sea ice initially covers half of the ocean surface, on the positive values of y, so that brine is rejected mainly on the other side of the domain, where there is extraction of buoyancy. A mixed-layer front develops along the sea ice edge, located at y = 0, where the instability grows.

Experiment	$T_{atm}$	Rotation/Eddies
REF	−20 °C	
REF-2D		No eddies
REF-NOROT		No rotation, no eddies
TWEAK	0°C	
TWEAK-2D		No eddies
TSTRONG	−40 °C	
TSTRONG-2D		No eddies

Table 1. Experiment names and characteristics. If not explicitly mentioned, the Coriolis parameter is  $f = 1.4 \times 10^{-4} \text{ s}^{-1}$  and the experimental domain is 3D, thus allowing eddies to form. The "no eddies" experiments are obtained via 2D simulations, while the Earth rotation is neglected by imposing f = 0.

the MITgcm (Winton 2000; Losch et al. 2010), simulating a single ice concentration and thickness at each grid point. Vertical mixing is realized by convective adjustment of buoyancy (without the convective vertical transport of horizontal momentum); we use the Smagorinsky scheme (Smagorinsky 1963) for horizontal viscosity with a standard coefficient value (Fox-Kemper and Menemenlis 2008), and there is no explicitly parameterized diffusion, only numerical upwinding.

The model domain (see Fig. 1) is a square channel (periodic in the along-ice-edge, x direction) with 30 vertical levels spaced at 2.5 meters. The horizontal grid spacing is 50 meters, with 1000 grid points on each side for a total side width of 50 km. This resolution allows us to resolve energy transfer across the inertial range. The initial atmospheric and oceanic conditions resemble a highly simplified wintertime Arctic Ocean. The ocean is initially at rest with a constant temperature near freezing of -1.8°C. The reference buoyancy structure of the domain is shown in Fig. 1. The mixed-layer (ML) is initialized to be of 25 meters depth, with a weak salinity-based stratification,  $\langle N^2 \rangle_{ML} = \langle \frac{\partial b}{\partial z} \rangle_{ML} \approx 0.5 \times 10^{-4} \text{ s}^{-2}$  (where  $\langle \cdot \rangle \equiv \langle \cdot \rangle^{xyz}$  stands for domain average in the x-y-z directions). At the mixed-layer base we impose a salinity jump of 0.4 psu, equivalent to a buoyancy jump  $\Delta b_0 \approx 3 \times 10^{-3} \text{ m/s}^2$ . This sets a stratification below the mixed-layer base of about  $10^{-3}$  s<sup>-2</sup>, at least one order of magnitude higher than the stratification in the ML, so that there is little intrusion of dense water into the deep ocean, and dynamics associated with brine rejection are confined to the mixed layer. The weak ML stratification implies a small ML deformation radius,  $L_d = NH/f \approx 2 \,\mathrm{km}$ , given a Coriolis parameter  $f = 1.4 \times 10^{-4} \text{ s}^{-1}$ . The whole-depth deformation radius is about 15 km, so there is little coupling between the mixed-layer eddies and whole-depth modes and the model results are not sensitive to our choice of the ocean depth. There is no solar forcing (approximating polar night), precipitation, or wind stress. A single sea ice edge bisects the domain into an ice-free region (negative y-axis, Fig. 1) and an ice-covered region (positive y-axis), creating a highly idealized sea ice geometry. Sea ice is initialized as grid cells with 100% ice concentration and a thickness of 2 meters. The initial domain-averaged sea ice concentration is thus 50%.

We design a set of experiments (see Table 1) so that we can isolate the different contributions to the dynamics, i.e., the effect of forcing, Coriolis and instabilities. In the REF run (Fig. 1)

the initial atmospheric temperature is  $T_{atm} = -20$  °C, leading to an initial net surface cooling around 200 W/m<sup>2</sup> and 50 W/m<sup>2</sup> in the ice-free region and in the ice-covered region of the domain, respectively. Due to the freezing ocean temperature, temperature fluxes are negligible and surface heat fluxes induce brine rejection and salinity fluxes solely. As a result, in a few hours new sea ice forms in the initially ice-free region, reaching a thickness of 7 cm in one day and almost 70 cm in 30 days; in the ice-covered region the sea ice thickens by almost 10 cm in 30 days. Thus, brine rejection is active in the whole domain and for the whole time of the simulation, but is heterogeneous in space and time. In addition to the REF experiment, we also perform a 2D simulation with no along-edge variability (REF-2D) to isolate the effects of baroclinic instability, as in Haney et al. (2012), and a 2D simulation where f = 0 (REF-NOROT) to isolate the effects of geostrophic flow (we performed a similar 3D experiment with f = 0 but found it gave the same results as the 2D experiment). These 2D runs help distinguish the role of mixed-layer eddies from pure geostrophic adjustment (see Fig. 2c). We perform two sensitivity experiments for forcing strength, either for initial temperatures of 0 °C (TWEAK; open-water cooling of 100 W/m<sup>2</sup>) and -40 °C (TSTRONG; open-water cooling of 500 W/m<sup>2</sup>), altering the rate of ice growth and brine rejection. We demonstrate an invariant scaling of buoyancy exchange across these large differences in air-sea fluxes (see Sec. 5b). All simulations are run for 30 days, by which time the eddies begin to interact with the domain boundaries. Over these time scales and for typical wintertime Arctic conditions, we assume atmospheric temperatures vary little, and sea ice thermodynamics alone drives upper ocean evolution. In order to reduce the complexity of the realistic ice-ocean interactions and only focus on a purely thermodynamic response, in these idealized configurations the sea-ice-ocean drag is explicitly absent. Ice-ocean drag has been explored in the more realistic discontinuous sea ice model studies of Gupta and Thompson (2022); Brenner et al. (2023).

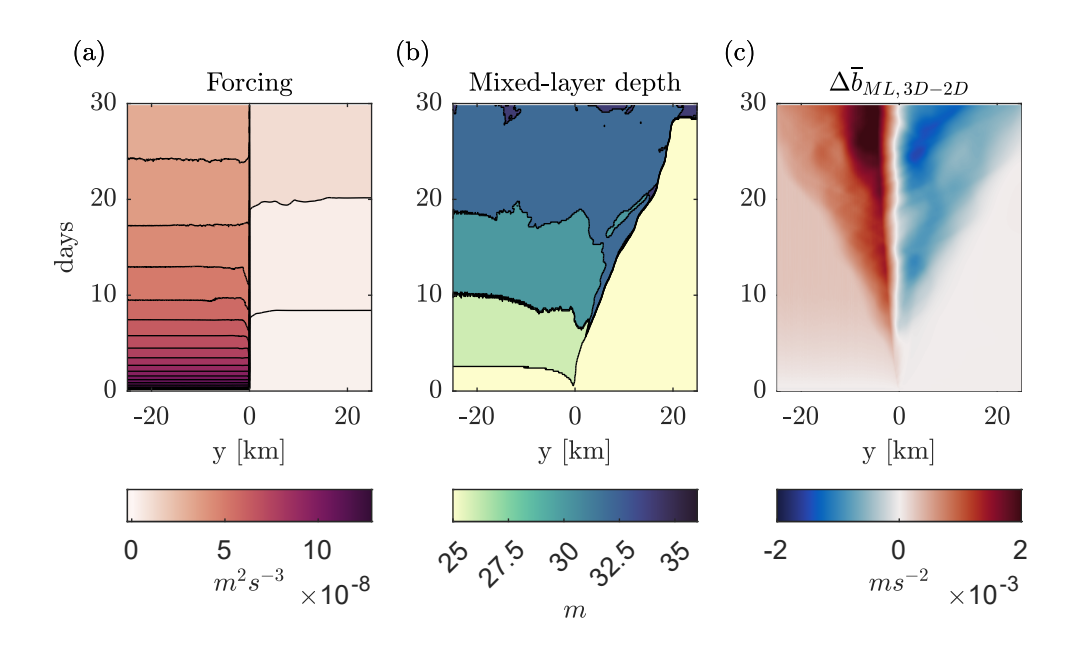


Fig. 2. Hovmöller diagrams of the along-ice-edge-average surface buoyancy flux (a), mixed-layer depth (b), and 3D-2D buoyancy (c) for REF.

## 3. Energetics

## a. Initial frontal dynamics and instability

Due to the different heat fluxes that arrive at the upper ocean in the ice-free and ice-covered regions, sea ice formation and brine rejection generate a cross-ice edge salinity front in the mixed layer (Fig. 1a). Gravity slumps the front via overturning currents in the across ice-edge direction, bringing lighter water from under the ice above denser water from the ice-free side, and releasing potential energy. In non-rotating simulations this gravitationally-driven overturning proceeds without an along-edge frontal flow. In the 2D, rotating simulations, along-edge currents balance the across-edge pressure gradient, tending toward a geostrophically-adjusted state which slowly adapts to continuing differential forcing (Ou 1984; Tandon and Garrett 1994), trapping potential energy from being released. In the 3D, rotating configurations this front is baroclinically unstable: meanders form along the sea ice-edge, growing into coherent submesoscale eddies in a few days. These facilitate the frontal overturning and conversion of lateral density gradients

into vertical stratification, and potential energy into eddy kinetic energy (Boccaletti et al. 2007, FFH).

The overturning processes occur continuously, as surface forcing continuously changes during the entire simulation time (see Fig. 2a) and acts to reinforce the density gradient. This is dynamically different from the initial condition frontal overturning problem studied in FFH, where the initial strength of the front is fixed and the front is then allowed to slump, and from MH, where the lead is artificially closed after a few days and the sea ice is treated as an ideal insulator. In our simulations, the freezing is not fast enough to trigger a strong superinertial wave response. The ice thickness and mixed-layer base isostatically continuously adjust, reducing gradients below the mixed layer and trapping most of the geostrophic shear and lateral buoyancy anomaly within the mixed layer.

The Hovmöller diagram of the along-edge average surface buoyancy flux is shown in Fig. 2a for REF. The average ice-free buoyancy flux  $(\dot{B})$  is nearly identical to the buoyancy flux difference between ice-free and ice-covered regions  $(\Delta \dot{B})$ ; for this reason we refer to  $\dot{B}$  in Sec. 4. As the brine is rejected, the ocean mixed-layer depth (MLD) increases in the ice-free region (Fig. 2b). Geostrophic adjustment and eddy overturning propagate the mixed-layer deepening under the ice and delineate the active frontal region. This mixed layer base adjustment is part of the process confining the geostrophic flow primarily within the mixed layer. In Fig. 2c we show a Hovmöller diagram of the difference in mixed-layer average buoyancy between the 3D and 2D REF simulations, which illustrates the impact of the eddies on the evolving geostrophic front. Over time, as the eddies emerge, the frontal region widens beyond geostrophic adjustment, increasing the lateral mixing of open-water-derived salinity. We explore the scaling of this widening, and its difference from standard geostrophic adjustment, in Sec. 4.

#### b. Energy cycle

Brine rejection leads to the injection of potential energy to the ocean domain, especially in the open-ocean region, following the surface forcing pattern in Fig. 2a. Not all the potential energy is available to be converted into kinetic energy since a majority sits at the base of the mixed layer, reinforcing the vertical stratification, and only a small fraction of the total potential

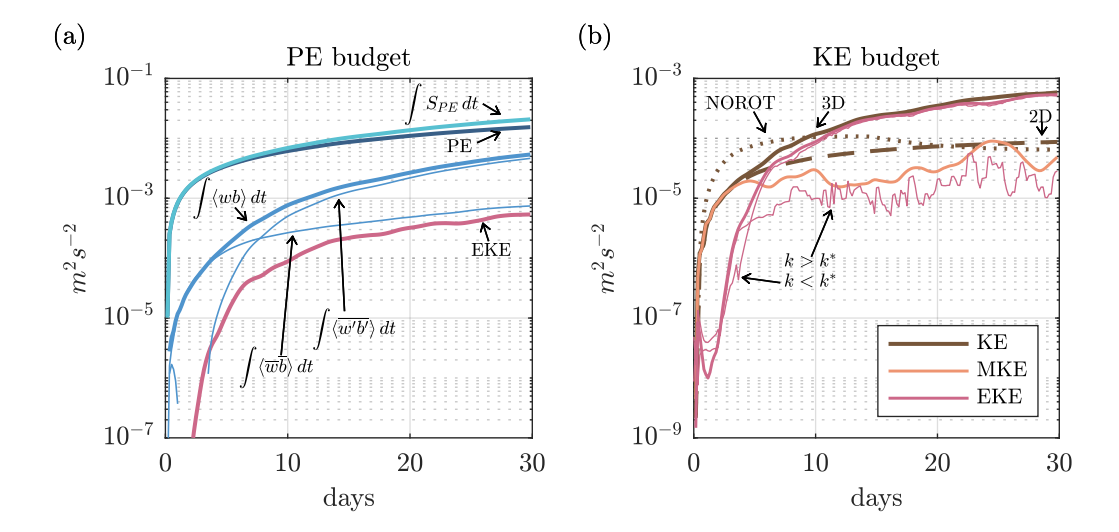


Fig. 3. Average potential energy (a) and kinetic energy (b) budgets for REF. (a)  $S_{PE}$ ,  $\langle wb \rangle$ ,  $\langle \overline{wb} \rangle$ , and  $\langle \overline{w'b'} \rangle$  are integrated in time in order to satisfy (2). Note that BPs are positive but represent sinks of PE. The EKE is also shown by the red line. (b) Kinetic energy (KE) (brown line) and its decomposition into mean (MKE) (orange line) and eddy part (EKE) (red line) for REF. Solid, dashed and dotted lines represent 3D, 2D and NOROT experiments, respectively. The EKE is then decomposed in the EKE in the inverse energy cascade ( $k < k^*$ ) and the EKE in the forward energy cascade ( $k > k^*$ ) (thinner red lines).

energy is localized along the front. Due to the complexity of directly diagnosing intermittent mixing and its effect on a continuously-forced available potential energy budget, we focus our attention on diagnosing the rate of change of overall potential energy, and connecting it to the evolution of kinetic energy. We keep the Boussinesq reference density  $(\rho_0)$  constant throughout the simulation, so that buoyancy changes are only due to forcing and dynamics, not a changing baseline:

$$b \equiv g \, \frac{\rho_0 - \rho}{\rho_0}.\tag{1}$$

For each variable, A, we define  $A = \overline{A} + A'$ , where  $\overline{(\cdot)}$  corresponds to the along-ice-edge average (i.e. average in x). The temporal evolution of the domain average potential energy (PE)

$$\frac{dPE}{dt} = -\frac{d}{dt}\langle zb\rangle = -\langle wb\rangle + S_{PE}$$

$$= -\langle \overline{wb}\rangle - \langle \overline{w'b'}\rangle + S_{PE},$$
(2)

where we define the domain average as  $\langle \cdot \rangle \equiv \langle \cdot \rangle^{xyz}$ . Sources and sinks have been separated into  $S_{PE} > 0$  and  $\langle wb \rangle > 0$ , respectively. This resembles the analysis of FFH with the addition of the source term  $S_{PE} = S_{PE}(t)$ , due to the continuous supply of PE from cooling which reinforces the front. The sink term is the average vertical buoyancy flux and may be separated into mean and eddy vertical buoyancy fluxes,  $\langle \overline{wb} \rangle$  and  $\langle \overline{w'b'} \rangle$ , which both tend to be positive (note that the vertical velocities implied by convective adjustment are not included in these terms, they represent only the resolved velocities; convective adjustment here contributes to  $S_{PE}$ ). We term these vertical buoyancy fluxes mean and eddy buoyancy production (mBP/eBP), since they represent source terms for the mean and eddy kinetic energy (MKE/EKE), respectively:

$$\frac{\partial MKE}{\partial t} = -\left\langle \frac{\partial}{\partial x_{j}} \left( \overline{u_{i}' u_{j}'} \overline{u_{i}} \right) \right\rangle - \left\langle \frac{\partial}{\partial x_{i}} \overline{u_{i}} \overline{\phi} \right\rangle + \left\langle \overline{w} \overline{b} \right\rangle + \left\langle \overline{u_{i}' u_{j}'} \frac{\partial \overline{u_{i}}}{\partial x_{j}} \right\rangle + D_{MKE},$$

$$\frac{\partial EKE}{\partial t} = -\left\langle \frac{\partial}{\partial x_{j}} \left( \frac{1}{2} \overline{(u_{i}')^{2} u_{j}} \right) \right\rangle - \left\langle \frac{\partial}{\partial x_{i}} \overline{u_{i}' \phi'} \right\rangle + \left\langle \overline{w' b'} \right\rangle - \left\langle \overline{u_{i}' u_{j}'} \frac{\partial \overline{u_{i}}}{\partial x_{j}} \right\rangle + D_{EKE}, \tag{3}$$

where, again,  $\overline{(\cdot)}$  and  $\langle \cdot \rangle$  stand for average in x and domain average (xyz), respectively. MKE and EKE themselves are the result of the x-average decomposition, so that the total domain average kinetic energy (KE) is defined as

$$KE = \frac{1}{2} \langle u_i^2 \rangle = \frac{1}{2} \langle \overline{u_i}^2 \rangle + \frac{1}{2} \langle \overline{u_i'}^2 \rangle \equiv MKE + EKE. \tag{4}$$

The RHS terms in (3) are respectively advection of kinetic energy (ADV), pressure gradient work (PW), buoyancy production (BP), shear production (SP), and dissipation of kinetic energy  $(D_{MKE}/D_{EKE})$ . When integrated over the whole domain, ADV and PW vanish as they are perfect derivatives without boundary sources. The buoyancy production  $\langle \overline{w}b \rangle$  is the mean

kinetic energy produced as the surface forcing provides dense water that is continually brought from the surface to the mixed-layer base;  $\langle \overline{w'b'} \rangle$  is the kinetic energy produced during baroclinic eddy development by a similar sorting process. The latter is the only buoyancy production acting in FFH because there is no continued surface forcing of density. Here  $\langle \overline{w'b'} \rangle$  is the more important buoyancy production, but both mean and eddy buoyancy production are continually growing. Shear production converts from MKE to EKE; we find that in the eddy regime SP is negligible, being, by day 15, 2 orders of magnitude smaller than BP.

Fig. 3a shows the potential energy budget for REF. The time-integrated  $S_{PE}(t)$  is obtained as a residual from (2), given PE and BP. As  $S_{PE}$  increases, the vertical eddy buoyancy flux,  $\langle \overline{w'b'} \rangle$ , grows. However, most of the potential energy accumulates rather than being converted to kinetic energy; it is difficult in this evolving situation to meaningfully define available potential energy.

KE is mainly governed by EKE once the eddies reach finite amplitude (Fig. 3b). Dashed and dotted brown lines in Fig. 3b compare against average KE for REF-2D and REF-NOROT, respectively. In the absence of eddies EKE is zero and thus KE is lower. KE is, however, initially more efficiently extracted from the density gradient along the ice edge in the absence of rotation as the flow is not restricted by geostrophy. In this case the absence of geostrophy leads, later on, to a faster re-stratification in the non-rotating case. In that case the front slumps more efficiently and KE attenuates after 10 days. The fact that in 2D experiments KE increases confirms that the front is continuously reinforced by brine rejection.

As in FFH, the vertical eddy buoyancy flux is the source of EKE. Yet, differently from FFH, no saturation level is reached by KE during the time of the simulation since the open-water source of density continuously increases the available potential energy. We discuss more about this in Sec. 5a.

## c. Energy cascade

Using the FFT algorithm, we compute the eddy kinetic energy spectrum as the 1D spectrum in the x-dimension, exploiting the natural periodicity and homogeneity in the x-direction and assuming isotropy in the perturbation fields, so that the 1D diagnosis represents the 2D spectral

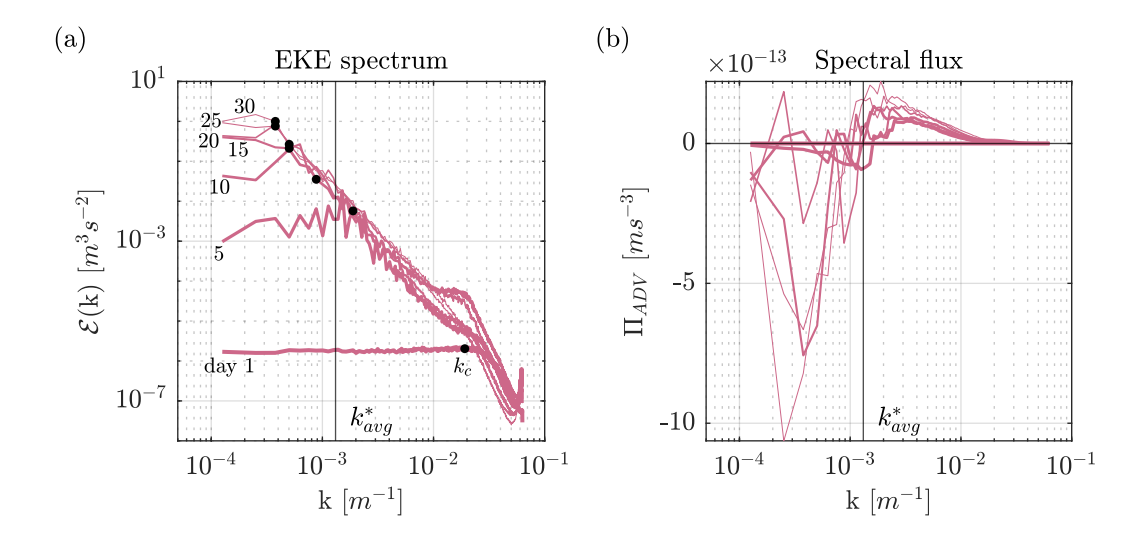


Fig. 4. (a) Time evolution of the EKE spectrum for REF experiment. Days 1, 5, 10, 15, 20, 25, and 30 are shown, with decreasing line thickness. The centroid wavenumber in (7) and the corresponding value of the spectrum is indicated by the black point marker for each day. (b) Corresponding spectral flux  $\Pi_{ADV}(k)$ . Same line thickness as in (a) for respective simulation time. For both (a) and (b),  $k_{avg}^*$  is the time average transition wavenumber distinguishing the forward and inverse energy cascades.

budget as well. The average EKE is related to the EKE spectrum via Plancherel's theorem:

$$EKE(t) = \frac{1}{2} \iiint (u^2 + v^2) dx dy dz$$

$$= \frac{1}{2} \iint \left( \int (|\hat{u}|^2 + |\hat{v}|^2) dk \right) dy dz$$

$$= \int \mathcal{E}(k, t) dk,$$
(5)

where

$$\mathcal{E}(k,t) = \frac{1}{2} \iint (|\hat{u}|^2 + |\hat{v}|^2) \, dy \, dz,\tag{6}$$

is the average EKE spectrum and  $\hat{u}(k, y, z, t) = \frac{1}{(2\pi)^{1/2}} \int u(x, y, z, t) e^{-ikx} dx$  is the Fourier Transform of the horizontal velocity field (u = (u, v)) in a hydrostatic model) in the wavenumber space in the x-direction, k. The behavior of the EKE spectrum in REF is shown in Fig. 4a. Low

wavenumbers are energized over time, showing that the energy is being transferred from the small scales to larger scales following an inverse energy cascade. The centroid wavenumber,

$$k_c = \frac{\int k\mathcal{E}(k)dk}{\int \mathcal{E}(k)dk} \equiv \frac{2\pi}{L_{eddy}},\tag{7}$$

indicated by the black point marker along the energy spectrum for each day shown in Fig. 4a, tracks the energy-containing length scale and confirms the inverse energy cascade tendency observed in Cohanim et al. (2021) for a brine-driven lead. We discuss the energy-containing eddy length scale,  $L_{eddy}$ , in Sec. 4.

Following Capet et al. (2008) and Cao et al. (2021), we define the eddy kinetic energy spectral flux,

$$\Pi_{ADV}(k) \equiv F_E \Big|_{k_{max}}^k = -\int_k^{k_{max}} \Re\left[\widehat{\boldsymbol{u}}^* \cdot \widehat{(\boldsymbol{u} \cdot \nabla)} \boldsymbol{u}\right] dk, \tag{8}$$

where  $F_E \Big|_{k_{max}}^k = F_E(k) - F_E(k_{max})$  is the energy flux due to non linear turbulent interactions from the wavenumber k through the largest wavenumber simulated,  $k_{max}$ , and the symbol  $\Re$  stands for the real part. The advective spectral flux shows a two-regime shape (Fig. 4b): positive for large wavenumbers, indicating there is a forward energy cascade at small length scales towards the dissipation scale, and negative for small wavenumbers, suggesting a transitioning behaviour toward a stronger inverse energy cascade, which intensities over time. The wavenumber at which  $\Pi_{ADV} = 0$  is the transition wavenumber  $k^*$ , which oscillates in time around an average value  $k_{avg}^* \approx 0.0013 \, \mathrm{m}^{-1}$  (vertical line in Fig. 4). Total EKE can be divided into the two regimes, that where  $k < k^*$ , the inverse energy cascade regime, and that where  $k > k^*$ , the forward energy cascade regime, which are shown as thin lines in Fig. 3b. Again, EKE is energized predominantly via the inverse energy cascade.

## 4. Scale analysis

The goal of this section is to study the behaviour of typical length scales of the brine-driven dynamics at a sea ice edge.

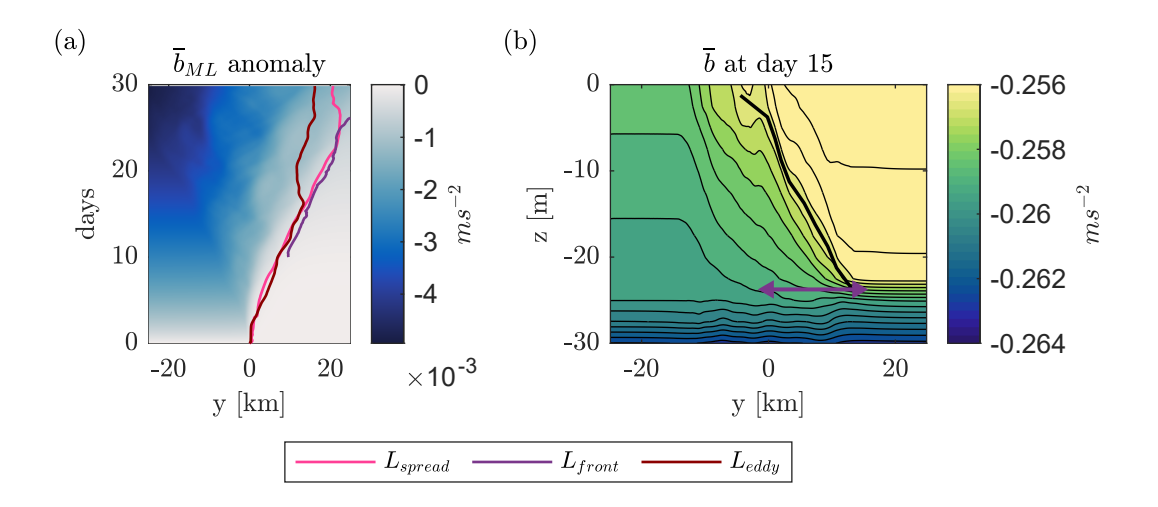


Fig. 5. Visualization of the definitions of the length scales  $L_{spread}$  (a) and  $L_{front}$  (b). (a)  $L_{spread}$ ,  $L_{front}$ ,  $L_{eddy}$  superimposed on the Hovmöller diagram of the ML average buoyancy anomaly from initial condition for REF. (b) Along-ice-edge average isopycnals (contour lines) and buoyancy (colors) for REF at day 15. The mean-surface-value isopycnal is marked by the thick black line and the horizontal distance  $L_{front}$  is indicated by the purple line.

#### a. Definition of typical length scales

MH suggest a scaling for the horizontal eddy diffusion under an idealized refreezing lead based on buoyancy conservation and the assumption that the lateral length scale is approximately the deformation radius,

$$L_d = \frac{NH}{f} \approx \frac{\sqrt{\Delta b \, H}}{f},\tag{9}$$

where  $\Delta b$  is the buoyancy difference across the front in the mixed layer of depth H. When the deformation radius is small compared to the lead width, the MH scaling is

$$L_{MH} = \frac{\sqrt{\dot{B}t}}{f},\tag{10}$$

where  $\dot{B}$  is the buoyancy flux in the opening (constant in their experiments and measured in  $m^2s^{-3}$ ) and t is the time the lead has been open. Note that (10) assumes no buoyancy flux through the ice.

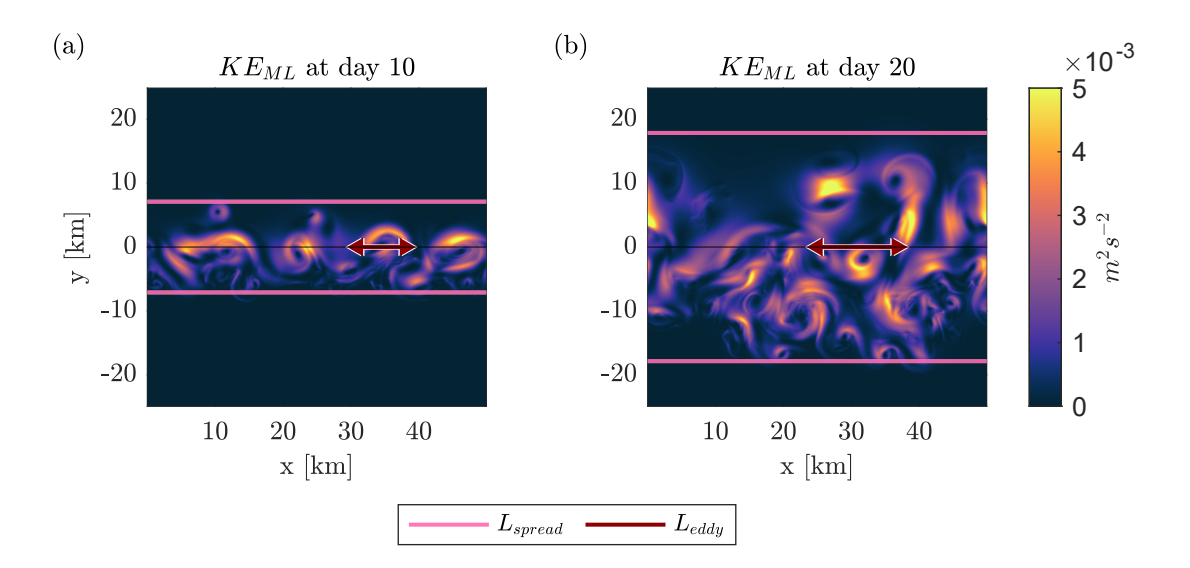


Fig. 6. Mixed layer kinetic energy at days 10 (a) and 20 (b) for REF.  $L_{spread}$  is represented by the pink lines as distance from the sea ice edge in the initially ice-covered (positive y-axis) and ice-free (negative y-axis) regions.  $L_{eddy}$  indicates the size of the most energetic eddy, marked by the dark red distance along the sea ice edge.

Here, because of the semi-infinite "lead" geometry, we are in the small deformation radius limit, so that (10) can be adopted. We assume H = H(t = 0), constant, even though the mixed-layer depth varies in time (Fig. 2b), since we find that the error introduced by this approximation is negligible. We find that  $L_{MH} \approx L_d$  (brown and orange solid lines, Fig. 7a). The small deviation of  $L_{MH}$  from  $L_d$  is due to the difference between  $\dot{B}$  (average ice-free buoyancy flux; flux we use for computing the MH scaling as in (10)) and  $\Delta \dot{B}$  (buoyancy flux difference between ice-free and ice-covered regions; actual average flux leaving the whole domain) (see Sec. 3a, Fig. 2a): MH use a constant surface forcing that is zero under the ice. Note that in our study, given the time-dependent forcing, the buoyancy difference across the front is

$$\Delta b(t) = \frac{1}{H} \int_0^t \Delta \dot{B}(\tau) d\tau \approx \frac{1}{H} \int_0^t \dot{B}(\tau) d\tau, \tag{11}$$

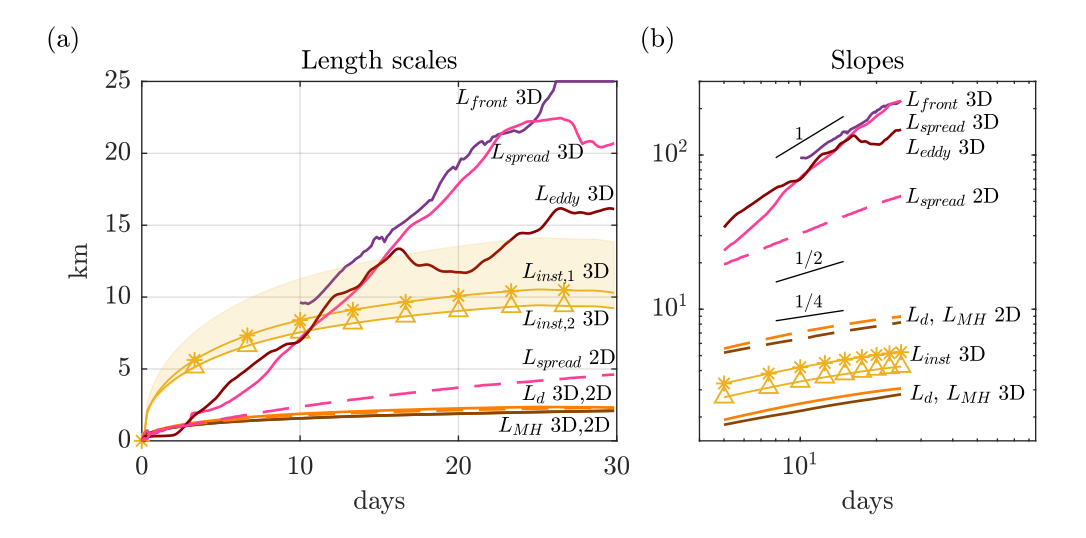


Fig. 7. (a) Typical length scales for REF (3D, solid lines) and REF-2D (dashed lines):  $L_{MH}$  (brown line),  $L_{d}$  (orange),  $L_{inst}$  range and measures 1 and 2 (yellow shade and lines),  $L_{eddy}$  (dark red),  $L_{spread}$  (pink),  $L_{front}$  (purple). (b) Same as (a) but with re-scaled y-axis in the range 5-25 days to compare with 1-, 1/2- and 1/4-slopes.

which reduces to the equality  $\Delta b(t) = \dot{B}t/H$  for constant  $\dot{B}$  flux, so that  $L_{MH} \approx L_d$  even in our time-dependent forcing case. Given the only dependence on the external forcing,  $L_{MH}$ , and thus  $L_d$ , are both similar for REF and REF-2D (solid and dashed lines in Fig. 7a). This result suggests that geostrophic adjustment of the 2D configuration including a growing deformation radius is insufficient to explain the 3D internal dynamics including MLEs, i.e., the 2D  $L_{MH} \approx L_d$  is not an accurate scaling for the lateral eddy diffusivity length. Note that the MH scaling, originally derived for a lead configuration (also under idealized conditions), is here used in its small-deformation-radius case for a semi-infinite "lead", and further efforts are needed to assess its validity in the small-lead-width case for a two coupled sea-ice edges geometry under continuous brine rejection.

We next compute complementary new scalings to describe the eddy-enhanced frontal overturning. We define  $L_{spread}$  as the expansion of the mixed-layer average buoyancy anomaly under the sea-ice (see pink line in Fig. 5a) by fitting the ML zonal-average buoyancy anomaly from the initial condition to a linear function for each simulation time. The frontal distance from the sea-ice edge,  $L_{front}$ , is instead computed by tracking the slope of the zonal-average isopycnal corresponding to the mean buoyancy value at the surface,  $\overline{b}^{xy}|_{z=0}$  (see purple line in Fig. 5b). When measuring  $L_{front}$ , we exclude values obtained at the early evolution of the front where such fitting is not possible. The comparison of  $L_{spread}$  and  $L_{front}$  is shown in Fig. 5a and Fig. 7a: the two metrics match well until the frontal expansion reaches the domain boundaries.  $L_{spread}$  derived in the 2D case (dashed pink line in Fig. 7a) grows significantly less than the 3D one because of the lack of eddy propagation and eddy dispersion of buoyancy into the under-ice region. Still, the 2D experiment expands more than would be suggested by the deformation radius alone, because of a cross-front 2D ageostrophic circulation associated with frontogenesis in the absence of submesoscale eddies. The MH length scale underestimates both the 2D-only and the 3D-eddy-affected expansion.

Following (7) we also compute the length scale of the centroid wavenumber, the eddy length scale,  $L_{eddy}$ .  $L_{eddy}$  tracks the scale of the most-energy-containing eddy and is shown as a dark red line in Fig. 7a. While this evolves in line with the spread of the mixed-layer average density ( $L_{spread}$ ), it appears to saturate at a constant size by day 15 for REF. In Fig. 5a we compare  $L_{spread}$ ,  $L_{front}$ , and  $L_{eddy}$ , showing that the front continues to evolve even as the energy-containing eddy length scale saturates. A visual comparison of  $L_{spread}$ , distance of frontal overturning, and  $L_{eddy}$ , eddy size, is also shown in Fig. 6: at day 10 they are of the same size, at day 20  $L_{spread} > L_{eddy}$ . This suggests that, at first, the eddies meander along the ice edge and grow in size, contributing to the frontal overturning, then, when they reach a saturation length scale, they start propagating away from the ice edge and the frontal spread is due to their displacement.

Finally, we examine the fastest growing mode of MLEs (Dong et al. 2020),

$$L_{inst} \approx 4\sqrt{1 + Ri^{-1}} L_d, \tag{12}$$

where

$$Ri = \frac{N^2}{\left(\frac{\partial \overline{u}_g}{\partial z}\right)^2} = \frac{N^2 f^2}{M^4} \approx \frac{\Delta y^2 f^2}{\Delta z \Delta b}$$
 (13)

is the Richardson number,  $N^2 = \frac{\partial b}{\partial z}$  and  $M^2 = \frac{\partial b}{\partial y}$  are the vertical and horizontal buoyancy gradients, and  $\Delta y$  and  $\Delta z = H$  are the horizontal and vertical length scales of the front. We examine two potential values for the instability length scale depending on the choice of  $\Delta y$ . For  $L_{inst,1}$ , we select  $\Delta y \approx 2L_d$  (Ri = O(1)), and for  $L_{inst,2}$ , we select  $\Delta y \approx 2L_{front}$  ( $Ri \gg O(1)$ ). Both solutions are shown in Fig. 7a as yellow solid lines with star and triangle markers, respectively, and belong to the range of typical values of  $L_{inst}$ ,  $4L_d \leq L_{inst} \leq 6L_d$  (yellow shaded area, Dong et al. 2020). These instability scales are smaller than  $L_{eddy}$ , but energy is transferred to larger scales by the inverse cascade shown in Fig. 4.

### b. Time evolution of frontal length scales

We here explore the time evolution of the different length scales defined in Sec. 4a. In Fig. 7b each length scale is re-scaled for visualization purposes, and we have included  $\sim t^1$ ,  $\sim t^{1/2}$ , and  $\sim t^{1/4}$  temporal scalings for reference.

The two buoyancy-fit-based metrics,  $L_{spread}$  and  $L_{front}$ , follow a near-linear expansion in time over the time period of eddy development, up until day 25 (for REF) when the frontal expansion reaches the domain boundary.

The two geostrophic metrics,  $L_d$  and  $L_{MH}$ , instead, follow a  $t^{\alpha}$  scaling law, with  $\alpha$  in between 1/4 and 1/2. We note that the fact that  $\dot{B}$  is evolving in time almost as  $t^{-1/2}$  in the 5-25 days range, and is not constant as in MH, causes the  $t^{1/2}$  power law to overestimate our geostrophic length scale.  $L_d$  and  $L_{MH}$  underestimate the continuously-forced geostrophic expansion ( $L_{spread} \sim t^{1/2}$  in REF-2D, pink dashed line), and its enhancement by the instability-driven mixing (pink line). Quantitatively, by day 15 they indicate an expansion less than 1/5 of what is observed due to the dynamical evolution of the ocean.

Given the proportionality to the deformation radius, also  $L_{inst}$  does not match correctly with the expansion of the front, exhibiting a power law temporal growth with exponent  $\alpha < 1/2$ .

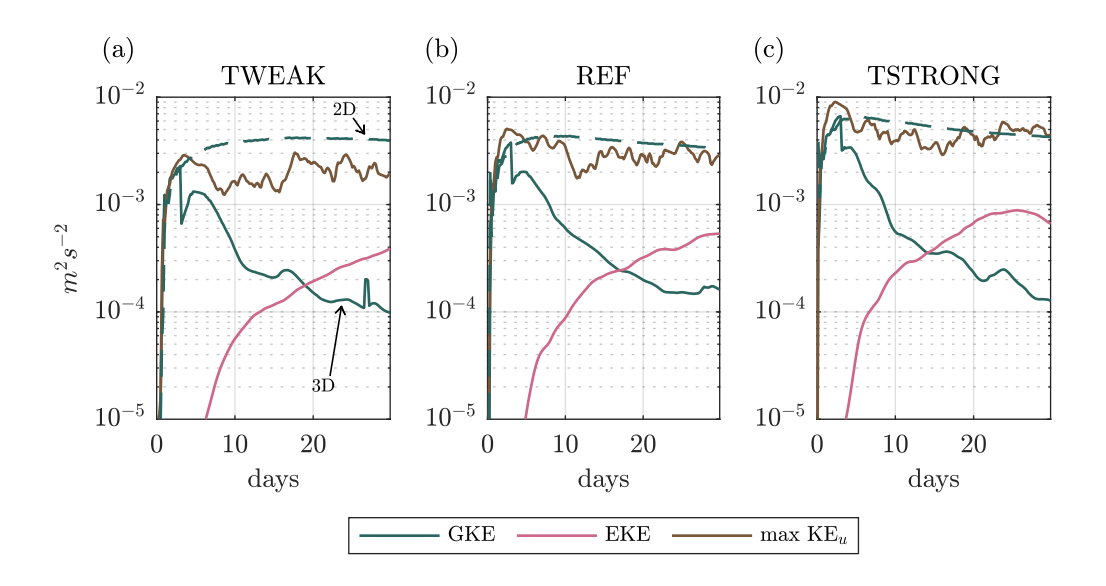


Fig. 8. Comparison of geostrophic kinetic energy scale (GKE, green line), eddy kinetic energy (EKE, red line) and the maximum zonal-mean KE of the velocity in the along-edge direction (brown line). Solid lines refer to 3D experiments, dashed lines to 2D experiments. TWEAK, REF and TSTRONG in panels (a), (b) and (c), respectively.

During the first several days,  $L_{inst}$  overestimates the spread of the density into the under-ice region, likely because of the early-stage dominance of shear production. Later on, once the baroclinic eddies emerge and grow,  $L_{inst}$  underestimates the rate of lateral buoyancy expansion  $L_{spread}$ . We do note, however, that at its upper bound  $(6L_d)$ ,  $L_{inst}$  matches the saturated  $L_{eddy}$ , reinforcing the physical interpretation of  $L_{inst}$  as the length scale of the fastest growing mode, or, equivalently, the scale of the energy-containing eddy. Still, a deeper analysis on the relationship between centroid wavenumber and fastest growing mode on longer integration times is required in order to validate the effectiveness of (12) in describing the energy-containing length scales of this continuously forced system.

#### 5. Discussion

#### a. The frontal adjustment velocity scale of FFH

The parameterization of mixing due to submesoscale eddies (MLEs) relies upon an assumption that the geostrophic velocity shear sets an upper bound to the EKE velocity scale. FFH show that the rms eddy velocity ( $\sqrt{2}$  EKE) saturates at the initial mean flow velocity, which is from geostrophy

$$U_g = \frac{M^2 H}{f}. ag{14}$$

Here we show that this condition is not satisfied in the continuously forced frontal adjustment problem, thus requiring a new approach to the ML restratification parameterization.

We compute (14) as

$$U_g \approx \frac{\Delta b H}{\Delta y f} \approx \frac{L_d^2}{2 L_{spread}} f,$$
 (15)

exploiting the scale analysis we performed in Sec. 4 by associating to the horizontal buoyancy gradient  $M^2$  the meaning of horizontal buoyancy variation across the frontal region, so that  $\Delta y \approx 2L_{front} \approx 2L_{spread}$ , and by using the deformation radius definition in (9). The background geostrophic velocity (15) is a function of the frontal width and deformation radius, or, equivalently, of the frontal width and of the surface forcing,  $U_g(t) = U_g(L_d(t), L_{spread}(t)) = U_g(\dot{B}(t), L_{spread}(t))$ . The geostrophic kinetic energy associated to the mean thermal wind  $U_g$  is

$$GKE = \frac{1}{2}U_g^2,\tag{16}$$

shown for REF and REF-2D by the solid and dashed green lines in Fig. 8b. Differently than FFH where the frontal strength is initially imposed and then all subsequent evolution of GKE scales with the initial value, here GKE is time dependent not only during evolution but also as the front is constructed by surface fluxes. Thus, GKE reduces as the front widens (and  $L_{spread}$  increases) in the eddy regime in both cases (FFH and this work), but there is no initial state governing this development in the ice edge case. The eddies act to reduce the vertical shear via horizontal mixing more efficiently than in 2D experiments. In Fig. 8b we also show EKE (red

line) and the maximum value of the zonal-mean kinetic energy  $\overline{u^2}_{max}/2$  (brown line). Recall that, as the forcing grows in time, despite the frontal adjustment process, the mean flow never grows to balance the cross-edge buoyancy gradient, and the EKE quickly grows, accounting for the majority of the ocean kinetic energy (Fig. 3b). Thus, at some time, EKE and GKE intersect (Fig. 8b), but the GKE at this point is dependent on the action of the eddies and only a circular argument relates GKE to EKE, so that we conclude that GKE is not a constraint for the evolution of the EKE in the ice edge case. Now we note that the maximum KE is stationary and higher than EKE, implying that the distribution of the zonal-velocity variance across the sea ice edge broadens over time with constant peak located in the frontal region, to allow for the total energy to increase with time. As the KE distribution gets wider, GKE decreases consistently with the widening of the frontal region. All of this is true also for the other experiments considered in Table 1 (Fig. 8a-c). A deeper analysis of the effects of different forcing conditions is performed in Sec. 5b.

To conclude, here we see that the brine-driven eddy frontal overturning is inherently different from the initial condition frontal spin-down considered by FFH. Given the nature of the time dependent background geostrophic velocity under brine rejection, submesoscale eddies forming at high latitudes because of lead-opening differ substantially from those forming at the mid latitudes and for which the MLE parameterization has been developed (Fox-Kemper et al. 2011).

#### b. Sensitivity to external forcing

The atmospheric temperature sets the buoyancy flux, and, thus, the brine rejection rate. Under different atmospheric temperatures, the frontal spread is also different. However, some aspects of the problem are independent on the atmospheric temperature, which we find by analyzing all of the experiments in Table 1 with the diagnostics studied for REF in Sec. 3-4. In particular, since the findings obtained for REF are valid for TWEAK and TSTRONG too, here we search for some non-dimensional variables that show a common behaviour among the different experiments. For some of them, we normalize the actual variables by their 2D solution,

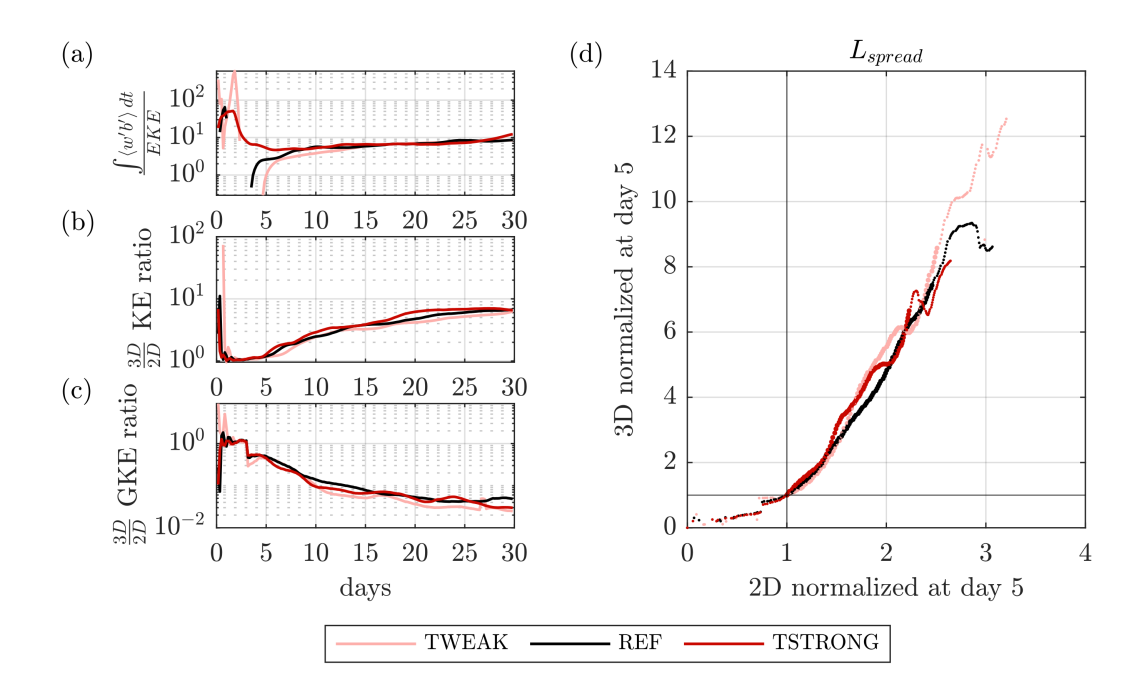


Fig. 9. TWEAK, REF, TSTRONG experiments comparison. (a) Production rate computed as the ratio between eBP and EKE. (b)-(c) Kinetic energy and geostrophic kinetic energy ratios between 3D and 2D experiments. (d) Scatter plot of the 3D vs 2D frontal spread length scale,  $L_{spread}$ . Each measure is normalized by its value at day 5 and the time window 5-20 days is highlighted by bigger marker sizes.

such that they are independent on the atmospheric temperature; recall that despite the same time-dependent forcing  $\dot{B}$ , 3D and 2D cases are fundamentally different (Sec. 3-4).

Fig. 9a shows the kinetic energy production rate computed as the ratio of the time integrated eddy buoyancy flux,  $\int \langle \overline{w'b'} \rangle dt$ , and the eddy kinetic energy, EKE, following (3). The eddy buoyancy production tends asymptotically to 10 times the EKE, independently on the external forcing. In Fig. 9b-c we normalize the kinetic energy KE and the geostrophic kinetic energy GKE in (16) by their values in the non-eddy-permitting simulations and we observe a common behavior for TWEAK, REF and TSTRONG. The GKE ratio also informs about the horizontal frontal displacement scaling, since, given (15),

$$\frac{GKE_{3D}}{GKE_{2D}} = \left(\frac{L_{spread,2D}}{L_{spread,3D}}\right)^{2}.$$
(17)

Again, we note that as KE increases with time, GKE decreases (Sec. 5a), since  $L_{spread}$  gets bigger in the 3D vs 2D experiments. These findings reinforce the idea of a proportionality law, once the non-eddy-dependent frontal adjusted solution is known. Finally, in Fig. 9d we explore the spread of the frontal region via the scatter plot of 3D vs 2D  $L_{spread}$ , normalized by its value at day 5, so that we can better compare the experiments under different forcing: the three experiments follow the same rate of growth with respect to their 2D frontal overturning.

To conclude, we find a uniform behavior for the eddy-induced frontal growth and horizontal transfer: when properly normalized, the different experiments collapse under the same laws. This lays the foundation for a non-dimensionalization toward the development of a new parameterization of the lateral transfer of buoyancy anomaly under sea ice.

#### 6. Summary and conclusions

Here, in a series of idealized numerical simulations, we examine the dynamics of sub-mesoscale baroclinic eddies that develop at a single sea-ice edge due to brine rejection. We show that the scaling of eddy transport of brine underneath the sea-ice edge is faster and broader than previously considered scaling laws based on estimates of the eddy size or geostrophic adjustment. The eddy kinetic energy also fails to saturate in time. We find the continuously-forced ice-edge problem is therefore fundamentally different from the standard frontal spindown experiments used to derive parameterizations of mixed layer eddies (FFH), and the role and energization of submesoscale eddies in the Arctic is likely different than in the ice-free oceans.

Through scale analysis we find that the distance of lateral buoyancy propagation deviates from the MH scaling and obeys instead a near linear evolution in time. Following Capet et al. (2008), the bulk of the eddy energy is found to cascade inversely, i.e., from the small scales to the large scales, and we can estimate the eddy scale via the centroid wavenumber, which evolves as the instability length scale (Dong et al. 2020) once the eddies become coherent vortices. At first the eddy length scale matches the lateral expansion of buoyancy, but once the eddies propagate away from the ice edge, they expand the lateral propagation of buoyancy beyond the typical unstable length scales. One of the core assumptions in the FFH MLE parameterization is not valid: that the mean background geostrophic velocity,  $U_g$ , constrains the eddy velocity scale.

Estimating the evolution and mixing of polar oceans due to submesoscale eddies is critical for the development of new parameterizations and for supporting new observational campaigns. Here, as a first step in this direction, we study the sensitivity to the atmospheric temperature and we find common behavior for some important non-dimensional variables under different forcing conditions.

There are some experimental design simplifications in this study. Here we examine only domains resembling an infinite half-plane of ice-covered ocean attached to an infinite half-plane of open water. Thus, the domain size of the simulation makes an appearance in the quantification of available potential energy, the maximum size of frontal spreading, and other scalings for budget parameters. We do not diagnose the energy dissipation by numerical and explicit subgrid sources sufficiently to capture some aspects of the energy cascade and conversions from potential to kinetic energy. We consider idealized conditions, with no winds or sea ice motion, while atmospheric temperatures evolve via the atmospheric boundary layer model of Deremble et al. (2013). Here, the air-sea temperature-derived fluxes are not prescribed and evolve during the simulations, as opposed to scalings based on diagnostic fluxes within observations or coupled models. We restore their temperature on a weekly time scale, which creates a near-infinite reservoir of heat (similar to a prescription of fixed atmospheric temperature). This is akin to the assumption that air-sea exchange does not greatly affect the atmospheric boundary layer, which should be explored in coupled studies. Additionally, an important limitation of this work is the highly simplified sea ice configuration with no ice-ocean drag, that potentially affects the lateral frontal displacement in a realistic scenario. Shrestha and Manucharyan (2022) show that ice-ocean drag dissipates the eddy kinetic energy and propose an adjustment to the FFH parameterization which depends on sea ice concentration. The ice-ocean drag has also been explored in recent studies involving floe-like geometries (Gupta and Thompson 2022; Brenner et al. 2023).

The aim of this paper is to develop the fundamental background for understanding the problem of continuously strongly-forced mixed-layer eddies. While we observe coherent scaling laws in eddy evolution that could be used to begin to recast FFH under the polar oceans, we note that

the simulation performed here is of a single sea ice edge, and not a single lead (a double ice edge). Thus, we do not prescribe an alternative parameterization to FFH yet, as the dynamics of two ice edges will be markedly different.

A further set of experiments, focusing on finite-size phenomena (i.e., leads) will be the focus of a following paper. Motivating our interest in finite-width leads is the observation of power-law type behavior in lead width, length, and duration (Marcq and Weiss 2012; Wernecke and Kaleschke 2015). Future work will consider how lead width affects the length scales of buoyancy injection and the expansion of buoyancy under the ice. We expect the wide lead case to behave similarly to the single ice edge. In particular, we will assess the scaling laws we define here and their relationship to sea-ice geometric variability, like lead size and duration of opening, using the idealized single-edge system to highlight how differences between FFH, MH, and the scaling identified here can be applied to an Arctic system in the context of the highly variable, multi-scale features.

Acknowledgments. All authors on this project are supported through the Scale Aware Sea Ice Project (SASIP). SASIP is supported by Schmidt Futures, a philanthropic initiative that seeks to improve societal outcomes through the development of emerging science and technologies. CH has partial support from NSF OPP-2146889 and thanks the National Institute of Water and Atmospheric Research in Wellington New Zealand for hospitality during parts of this work. ALP and BFK have partial support from NSF 2149041. Computing resources were provided by NSF 1655221.

Data availability statement. Simulation data and analysis software is available on the Brown Digital Repository at https://doi.org/10.26300/ak1p-2v10.

## References

Aagaard, K., and E. C. Carmack, 1989: The role of sea ice and other fresh water in the Arctic circulation. *Journal of Geophysical Research*, **94** (**C10**), 14485.

Biddle, L. C., and S. Swart, 2020: The Observed Seasonal Cycle of Submesoscale Processes in the Antarctic Marginal Ice Zone. *Journal of Geophysical Research: Oceans*, **125** (6).

- Boccaletti, G., R. Ferrari, and B. Fox-Kemper, 2007: Mixed Layer Instabilities and Restratification. *J. Phys. Oceanogr.*, **37** (9), 2228–2250.
- Bodner, A. S., B. Fox-Kemper, L. Johnson, L. P. Van Roekel, J. C. McWilliams, P. P. Sullivan, P. S. Hall, and J. Dong, 2023: Modifying the mixed layer eddy parameterization to include frontogenesis arrest by boundary layer turbulence. *Journal of Physical Oceanography*, **53** (1), 323–339, https://doi.org/10.1175/JPO-D-21-0297.1.
- Brenner, S., C. Horvat, P. Hall, A. Lo Piccolo, B. Fox-Kemper, S. Labbé, and V. Dansereau, 2023: Scale-dependent air-sea exchange in the polar oceans: Floe-floe and floe-flow coupling in the generation of ice-ocean boundary layer turbulence. *Geophysical Research Letters*, **50** (23), e2023GL105703, https://doi.org/https://doi.org/10.1029/2023GL105703, https://agupubs.onlinelibrary.wiley.com/doi/pdf/10.1029/2023GL105703.
- Brenner, S., L. Rainville, J. Thomson, and C. Lee, 2020: The evolution of a shallow front in the Arctic marginal ice zone. *Elem Sci Anth*, **8** (1), 17.
- Bush, J. W., and A. W. Woods, 2000: An investigation of the link between lead-induced thermohaline convection and arctic eddies. *Geophysical Research Letters*, **27** (**8**), 1179–1182.
- Callies, J., and R. Ferrari, 2013: Interpreting Energy and Tracer Spectra of Upper-Ocean Turbulence in the Submesoscale Range (1–200 km). *Journal of Physical Oceanography*, **43** (11), 2456–2474.
- Cao, H., B. Fox-Kemper, and Z. Jing, 2021: Submesoscale Eddies in the Upper Ocean of the Kuroshio Extension from High-Resolution Simulation: Energy Budget. *Journal of Physical Oceanography*, **51** (**7**), 2181–2201.
- Capet, X., J. C. McWilliams, M. J. Molemaker, and A. F. Shchepetkin, 2008: Mesoscale to submesoscale transition in the {California} current system. {Part III}: Energy balance and flux. *Journal of Physical Oceanography*, **38** (**10**), 2256–2269.
- Cohanim, K., K. X. Zhao, and A. L. Stewart, 2021: Dynamics of Eddies Generated by Sea Ice Leads. *Journal of Physical Oceanography*, **51** (**10**), 3071–3092.

- Deremble, B., N. Wienders, and W. K. Dewar, 2013: CheapAML: A Simple, Atmospheric Boundary Layer Model for Use in Ocean-Only Model Calculations. *Monthly Weather Review*, **141** (2), 809–821.
- Dong, J., B. Fox-Kemper, H. Zhang, and C. Dong, 2020: The seasonality of submesoscale energy production, content, and cascade. *Geophysical Research Letters*.
- Fily, M., and D. A. Rothrock, 1990: Opening and closing of sea ice leads: Digital measurements from synthetic aperture radar. *Journal of Geophysical Research*, **95** (C1), 789.
- Fox-Kemper, B., R. Ferrari, and R. Hallberg, 2008: Parameterization of Mixed Layer Eddies. Part I: Theory and Diagnosis. *Journal of Physical Oceanography*, **38** (6), 1145–1165.
- Fox-Kemper, B., and D. Menemenlis, 2008: Can large eddy simulation techniques improve mesoscale-rich ocean models? *Ocean Modeling in an Eddying Regime*, M. Hecht, and H. Hasumi, Eds., Vol. 177, AGU Geophysical Monograph Series, 319–338.
- Fox-Kemper, B., and Coauthors, 2011: Parameterization of mixed layer eddies. III: Implementation and impact in global ocean climate simulations. *Ocean Modelling*, **39** (**1-2**), 61–78.
- Giddy, I., S. Swart, M. du Plessis, A. F. Thompson, and S.-A. Nicholson, 2021: Stirring of Sea-Ice Meltwater Enhances Submesoscale Fronts in the Southern Ocean. *Journal of Geophysical Research: Oceans*, **126** (4), e2020JC016 814.
- Gupta, M., and A. F. Thompson, 2022: Regimes of sea-ice floe melt: Ice-ocean coupling at the submesoscales. *Journal of Geophysical Research: Oceans*, **127** (9), e2022JC018894, https://doi.org/https://doi.org/10.1029/2022JC018894, https://agupubs.onlinelibrary.wiley.com/doi/pdf/10.1029/2022JC018894.
- Haney, S., and Coauthors, 2012: Hurricane wake restratification rates of one-, two- and three-dimensional processes. *Journal of Marine Research*, **70** (6), 824–850.
- Herman, A., 2022: Granular effects in sea ice rheology in the marginal ice zone. *Philosophical Transactions of the Royal Society A: Mathematical, Physical and Engineering Sciences*, **380** (2235), 20210 260.

- Horvat, C., 2022: Floes, the marginal ice zone and coupled wave-sea-ice feedbacks. *Philosophical Transactions of the Royal Society A: Mathematical, Physical and Engineering Sciences*, **380** (2235), 20210 252.
- Horvat, C., E. Tziperman, and J.-M. Campin, 2016: Interaction of sea ice floe size, ocean eddies, and sea ice melting. *Geophysical Research Letters*, **43** (**15**), 8083–8090.
- Hutter, N., L. Zampieri, and M. Losch, 2019: Leads and ridges in Arctic sea ice from RGPS data and a new tracking algorithm. *The Cryosphere*, **13** (2), 627–645.
- Lindsay, R. W., and D. A. Rothrock, 1995: Arctic sea ice leads from advanced very high resolution radiometer images. *Journal of Geophysical Research*, **100** (**C3**), 4533.
- Losch, M., D. Menemenlis, J. M. Campin, P. Heimbach, and C. Hill, 2010: On the formulation of sea-ice models. Part 1: Effects of different solver implementations and parameterizations. *Ocean Modelling*, **33** (**1-2**), 129–144.
- Marcq, S., and J. Weiss, 2012: Influence of sea ice lead-width distribution on turbulent heat transfer between the ocean and the atmosphere. *The Cryosphere*, **6** (**1**), 143–156, https://doi.org/10.5194/tc-6-143-2012.
- Marshall, J., A. Adcroft, C. Hill, L. Perelman, and C. Heisey, 1997: Hydrostatic, quasi-hydrostatic and nonhydrostatic ocean modeling. *J. Geophys. Res.*, **102**, **C3**, 5733–5752.
- Matsumura, Y., and H. Hasumi, 2008: Brine-driven eddies under sea ice leads and their impact on the Arctic Ocean mixed layer. *Journal of Physical Oceanography*, **38** (1), 146–163.
- Mensa, J. A., and M.-L. Timmermans, 2017: Characterizing the seasonal cycle of upper-ocean flows under multi-year sea ice. *Ocean Modelling*, **113**, 115–130.
- Mensa, J. A., M.-L. Timmermans, I. E. Kozlov, W. J. Williams, and T. M. Özgökmen, 2018: Surface Drifter Observations From the Arctic Ocean's Beaufort Sea: Evidence for Submesoscale Dynamics. *Journal of Geophysical Research: Oceans*, **123** (4), 2635–2645.
- Ou, H. W., 1984: Geostrophic Adjustment: A Mechanism for Frontogenesis. *Journal of Physical Oceanography*, **14** (**6**), 994–1000.

- Rosenblum, E., R. Fajber, J. C. Stroeve, S. T. Gille, L. B. Tremblay, and E. C. Carmack, 2021: Surface Salinity Under Transitioning Ice Cover in the Canada Basin: Climate Model Biases Linked to Vertical Distribution of Fresh Water. *Geophysical Research Letters*, **48** (21).
- Schulson, E. M., 2004: Compressive shear faults within arctic sea ice: Fracture on scales large and small. *Journal of Geophysical Research C: Oceans*, **109** (**7**), C07 016.
- Shrestha, K., and G. E. Manucharyan, 2022: Parameterization of Submesoscale Mixed Layer Restratification under Sea Ice. *Journal of Physical Oceanography*, **52** (3), 419–435.
- Smagorinsky, J., 1963: General Circulation Experiments With the Primitive Equations. *Monthly Weather Review*, **91** (3), 99–164.
- Smith IV, D. C., J. W. Lavelle, and H. J. S. Fernando, 2002: Arctic Ocean mixed-layer eddy generation under leads in sea ice. *Journal of Geophysical Research: Oceans*, **107** (C8), 17–1–17–17.
- Smith IV, D. C., and J. H. Morison, 1998: Nonhydrostatic haline convection under leads in sea ice. *Journal of Geophysical Research: Oceans*, **103** (**C2**), 3233–3247.
- Steiner, N., and Coauthors, 2004: Comparing modeled streamfunction, heat and freshwater content in the Arctic Ocean. *Ocean Modelling*, **6** (3-4), 265–284.
- Swart, S., M. D. Plessis, A. F. Thompson, L. C. Biddle, I. Giddy, T. Linders, M. Mohrmann, and S.-A. Nicholson, 2020: Submesoscale Fronts in the Antarctic Marginal Ice Zone and Their Response to Wind Forcing. *Geophysical Research Letters*, **47** (6).
- Tandon, A., and C. Garrett, 1994: Mixed Layer Restratification Due to a Horizontal Density Gradient. *Journal of Physical Oceanography*, **24** (6), 1419–1424.
- Timmermans, M.-L., S. Cole, and J. Toole, 2012: Horizontal Density Structure and Restratification of the Arctic Ocean Surface Layer. *J. Phys. Oceanogr.*, **42** (**4**), 659–668.
- Wernecke, A., and L. Kaleschke, 2015: Lead detection in arctic sea ice from cryosat-2: quality assessment, lead area fraction and width distribution. *The Cryosphere*, **9** (**5**), 1955–1968, https://doi.org/10.5194/tc-9-1955-2015.

- Wettlaufer, J. S., M. G. Worster, and H. E. Huppert, 1997: The Phase Evolution of Young Sea Ice. *Geophysical Research Letters*, **24** (**10**), 1251–1254.
- Winton, M., 2000: A Reformulated Three-Layer Sea Ice Model. *Journal of Atmospheric and Oceanic Technology*, **17** (**4**), 525–531.